MODELLING SCATTERING DISTORTION IN 3D RANGE CAMERA

Sonam Jamtsho and Derek D. Lichti

Department of Geomatics Engineering, The University of Calgary
2500 University Dr NW, Calgary AB T2N 1N4, Canada
sjamtsho@ucalgary.ca, ddlichti@ucalgary.ca

Commission V, WG 3

KEY WORDS: Range camera, Scattering, Empirical Modelling, Spline Interpolation, Curve-fitting, Surface-fitting

ABSTRACT:

A time-of-flight camera suffers from significant range distortion due to the scattering artefact caused by secondary reflections occurring between the lens and the image plane. The reflected beam from the foreground objects undergoes multiple reflections within the camera device thereby introducing parasitic signals that bias the late-arrival, backscattered signals from the background targets. These additive signals cause degradation of the depth measurement for the background objects thus limiting the use of range imaging cameras for high precision close-range photogrammetric applications. So far the modelling of scattering distortion has been based on the linear system model using an inverse filtering approach. However, an experiment conducted for measuring the edge-spread function using a two planar surfaces separated at some distance shows a non-linear and shift-variant behaviour of the scattering distortion. The non-linearity and the shift-variant behaviour of the scattering errors question the use of the linear shift-invariant system for reversing the scattering effect. Further experimentation using two planar surfaces at different distances with different surface areas of the scattering object was conducted to heuristically quantify the range and amplitude biases caused by the scattering artefact. The range and amplitude biases were analysed as a function of the distance of the scattering object from the camera, the surface area of the scattering object and the integration time. The results show that the scattering bias monotonically increases with surface area of the scattering object and monotonically decreases with distance of the scattering object from the camera. The scattering range bias is independent of the integration time while the scattering amplitude bias monotonically increases with the integration time. Additionally, an empirical modelling of the range bias due to the scattering effect using an analytical curve-fitting method is proposed in this paper.

1. INTRODUCTION

Three-dimensional range imaging camera systems are a recent development for close-range terrestrial photogrammetric applications. They operate based on the phase-shift principle to determine the distance between the target and the camera. Each pixel in the sensor frame independently measures distance and amplitude information of the scene which is realized through CCD/CMOS lock-in pixel technology (Lange and Seitz, 2001).

Like any other digital imaging sensors, the 3D range cameras are biased with radiometric and geometric distortions. The systematic errors of time-of-flight (ToF) cameras range from standard camera distortions like radial and decentring distortions to more complicated range biases due to surface reflectivity (Falie and Buzuloiu, 2008), incidence angle (Karel et al., 2007), scattering artefact (Kavli et al., 2008; Mure-Dubois and Hugli, 2007), internal camera temperature and integration time (Kahlmann et al., 2006), amplitude attenuation (Jaakkola et al., 2008) and internal electronic noises (Lange, 2000). Research is underway for developing a calibration procedure for the range cameras by incorporating range measurements in a self-calibration approach (Robbins et al., 2009; Lichti, 2008) or by separately modelling the range distortions besides performing standard digital camera calibration (Chiabrando et al., 2009; Beder and Koch, 2008). However, the 3D range imaging cameras are not able to be efficiently calibrated due to imaging scene-variant scattering induced amplitude and range bias on the background objects.

Kavli et al. (2008) and Mure-Dubois and Hugli (2007) have published results on the compensation of scattering bias using an inverse filtering approach. They used a trial-and-error method to define the inverse filter based on a Gaussian or an empirically defined point-spread function (PSF) approximation. Nonetheless, the linear system model is questionable due to inhomogeneous multiple light reflections inside the camera system, and therefore may not be applicable for all scattering scene environments. Thus, in the absence of a general physical basis, the only alternative is to empirically model the scattering distortions through exhaustive experimentation.

The outline of this paper is as follows. Section 2 presents a brief description of the principle of the scattering effect in 3D range cameras. Section 3 describes the experiments used for measuring the scattering distortion and the scattering-induced range and amplitude biases as a function of different parameters for SR3000 and SR4000 range cameras. Section 4 describes the methodology of the scattering compensation model using an analytical curve-fitting approach and Section 5 presents the test results of the scattering compensation.

2. THE SCATTERING PHENOMENON

2.1 Principle of the Scattering Effect

In ToF cameras, the range information is obtained from measuring the time delay of the modulated received signal. The

phase-shift of the amplitude-modulated signal corresponds to the time delay of the signal received by the sensor. The range of the object from the sensor is calculated using Equation 1, where ρ is the range for a given pixel, λ is the modulation frequency, φ is the phase-shift of the received signal, and i, j is the pixel location.

$$\rho(i,j) = \frac{\lambda}{4\pi} \cdot \varphi(i,j) \quad (1)$$

The phase-shift for closer objects will be smaller than the phase-shift for the farther objects as shown in Figure 1, where A, B and C are the angular phase offsets, and the ρ_Q, $\rho_{Q'}$ and ρ_O are the corresponding ranges of the point Q, Q' and O respectively.

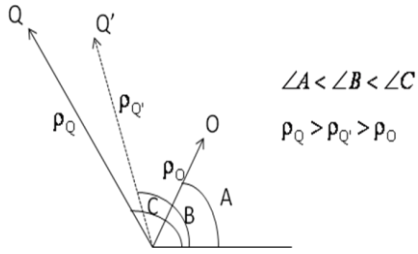

Figure 1: Angular phase offset and range measurement

The point Q' is the displaced point Q due to the scattering effect, which is caused by the presence of a highly reflective closer object O in the imaging scene. The scattering effect is caused by the occurrence of multiple internal reflections of the signals from the foreground object between the optical lens system and the image plane. The early-arrival signals from the foreground object attenuate the late-arrival weak signal from the background object. Hence the camera measures a lower angular phase offset for the signals from the background object which proportionally correspond to a shortened range measurement. However, the exact nature of multiple internal reflections of the signals is difficult to describe with a physical model because the scattering phenomenon is highly scene dependent. This poses a limitation to any perceived physical model for the scattering artefact in the 3D range cameras.

2.2 Limitation of the Linear System Model

According to Mure-Dubois and Hugli (2007), the scattering problem is expressed as a convolution of an input signal with the impulse response of the system in presence of the scattering bias. The solution to this problem explicitly requires modelling of the scattering PSF of the camera so that deconvolution can be employed to undo the effect of the scattering. The linear system model typically requires defining or measuring the PSF accurately in order to successfully undo the filtering operation. The above authors defined the point-spread function of the camera including scattering bias plausibly by a trial-and-error method using a Gaussian approximation. Kavli et al. (2008) also used linear system model to compensate for the scattering distortions in ToF cameras using "generally shaped empirical models" for the point spread function.

The direct measurement of the scattering PSF is impossible due to non-idealization of a point scattering object. Often the line spread function (LSF) or the edge spread function (ESF) is measured to deduce the PSF indirectly. It is possible to measure the ESF and deduce the scattering bias PSF, which is equal to the derivative of the scattering ESF.

An experiment using two planar objects was conducted to measure the ESF of the scattering effect. The range camera was placed at 1 m from the scattering object (plane board) and 2.5 m from the background object (wall). Image frames were captured with and without the presence of the scattering object. Figure 2 (Left) shows the intensity image of the ESF experiment and Figure 2 (Right) shows the superimposed point clouds of the scattering scene with and without the presence of the foreground scattering object. The long linear band of points is the point cloud of only the background object when the scattering object is not present, whereas the step-like band of points is the point cloud of both the background and scattering object. The displacement of the background wall towards the camera due to the presence of the foreground scattering object is caused by the scattering phenomenon.

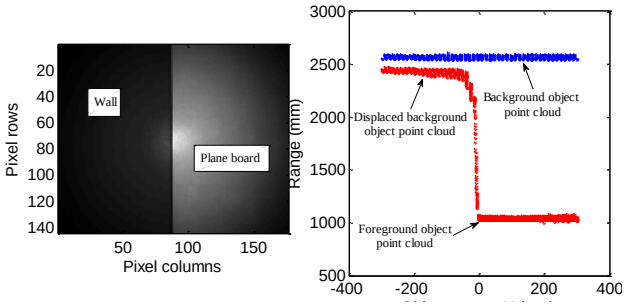

Figure 2: Intensity image (Left) and superimposed point clouds (Right)

Figure 3 shows the superimposed theoretical (dotted line) and measured ESF (solid line) obtained from the scattering experiment. The measured ESF was obtained by fitting a curve on one row pixel from the step-like band of points shown in Figure 2 (Right).

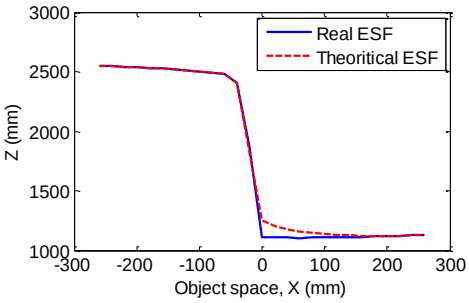

Figure 3: Edge spread function of a scattering distortion profile

The measured ESF does not conform to the expected theoretical ESF of the scattering distortion profile. This indicates that the scattering range bias deviates from the linearity assumption of the linear shift-invariant system. It will be also shown in the following section that the scattering effect is non shift-invariant because the scattering bias is highly dependent on the position of the foreground scattering object. Perhaps the linear system model does not accurately describe the scattering phenomenon in the 3D range cameras. In the absence of a concrete physical scattering model, it is imperative to explore the empirical methods of modelling scattering distortions through exhaustive experimentation, which is the subject of this paper.

3. MEASUREMENT OF THE SCATTERING EFFECT

3.1 Two Planar Objects Experiment

SR3000 and SR4000 range cameras were used for modeling the scattering artefact. A planar wall was imaged with and without the presence of another highly reflective foreground planar object. A white projector screen of size 2.4 m by 2.4 m was used as a foreground scattering object for this experiment. Figure 4 shows the experimental set up for the scattering imaging scene.

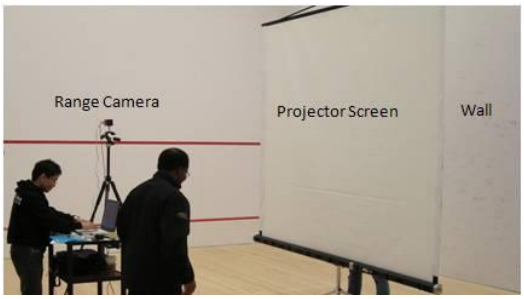

Figure 4: Set up for the scattering experiment

Five forward distance (longitudinal) positions were chosen at 1.4 m to 3.0 m with a 0.4 m interval from the range camera. Nine lateral positions were chosen at each forward distance location where images were taken with different percentage of surface area of the foreground object from 10% to 90% at a 10% interval. The experiment was conducted only up to 4.0 m of the camera's range because of the unavailability of a sufficiently large foreground planar object which is required to cover the whole sensor frame with the foreground object. At each location, twenty frames were captured to compute the mean value of the observables because the single image of the range camera is very noisy. Images were captured at four different integration times at 50, 120, 180 and 255 8-bit quantized values, which correspond to 10.2 ms, 24.2 ms, 36.2 ms and 51.2 ms respectively for SR3000 and 5.3 ms, 12.3 ms, 18.3 ms and 25.8 ms respectively for SR4000.

3.2 Scattering Effect on Range and Amplitude

3.2.1 SR3000 Range Camera

The scattering artefact in the range cameras is portrayed in the form of range and amplitude biases on the background objects. The measured range and amplitude for the background objects in the presence of a scattering foreground object are lower than the measurements without the presence of a scattering object. To distinguish from the x-coordinate of the ESF experiment, henceforth the x-coordinate refers to the image space of the camera. Figure 5 shows the range and amplitude biases of one central row of pixels as a function of the surface area of the scattering object. The camera and the background object were fixed at 3.8 m with the scattering object placed at different lateral positions at a distance of 1.8 m from the camera. The trend is clearly visible where the range and amplitude biases are increasing monotonically as a function of the surface area of the scattering object. This is expected because when the surface area of the scattering object is larger, more scattering is occurring inside the camera causing greater attenuation of the signals from the background object.

It is also observed that the range bias gradually decreases from the scattering edge towards the center of the image and then exponentially increases towards the periphery of the image. The scattering edge is located at the right end of the curves which is defined as the location of the edge of the foreground object, where the edge of the foreground object overlaps with the background object. Some portion of this additional bias at the periphery can be attributed to the power loss due to the vignetting effect of the lens. However, the range biases at the edges are not homogenous throughout the image frame, which indicates that there are other system errors influencing the scattering distortion.

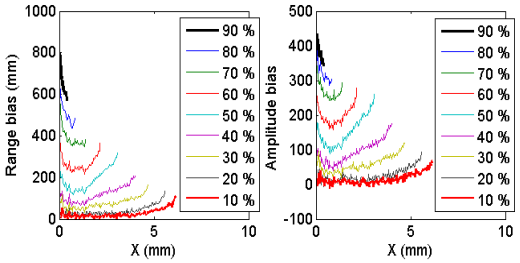

Figure 5: Scattering bias as a function of surface area of the scattering object

Further observation exposed the proportional dependence between the range and amplitude biases. It has been reported by Mure-Dubois and Hugli (2007) that the phase-shift due to scattering effect is proportional to the ratio ΔA/A. From Equation 1, it can be seen that the range bias is proportional to the phase-shift, therefore the range bias is also proportional to the ratio ΔA/A.

Figure 6 is the range and amplitude biases dependence plot using un-normalized and normalized amplitude bias. The amplitude bias (ΔA) is normalized with the amplitude (A) of the signal from the background object. Figure 6 (Left) is a linear fit of individual data of corresponding range and amplitude biases and the right image is the superimposed linear and polynomial fit of all data at different surface areas of the scattering object seen in Figure 5. It can be seen that the proportional dependence of the range and amplitude biases is true for the lower range biases but exhibits a monotonic increasing low-order polynomial relationship for the larger range biases.

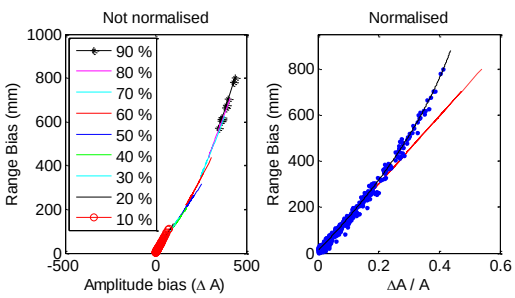

Figure 6: Amplitude and range bias dependence

Figure 7 shows the range and amplitude biases as a function of the integration time. This image was taken with the range camera placed at 1.8 m and 3.8 m from the scattering and background object respectively with 50% occlusion of the background object. All four integration times for the same scattering scene show very similar trends. This suggests that the scattering effect on range measurements is invariant to the integration time. However, the amplitude bias due to scattering is dependent on the integration time. The monotonic relationship between the integration time used and the

scattering-induced amplitude bias is because a greater number of photons impinge on the sensor at higher integration times.

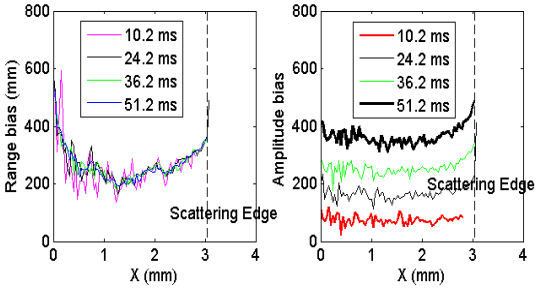

Figure 7: Scattering bias as a function of the integration time

Figure 8 portrays the range and amplitude biases as a function of the distance of the scattering object from the camera. These images were taken with the camera placed at 3.8 m from the background object and the scattering object placed at four different locations at 0.4 m increments starting at 1.4 m from the camera. It can be seen that the range and amplitude biases monotonically decrease with the distance of the scattering object from the camera. This is expected because the power of the signal decays as the inverse square of the distance. When the scattering object is closer to the camera relative to the background object, the reflected light from the scattering object has more power than the reflected light from the background object causing greater signal attenuation resulting in a proportional scattering bias.

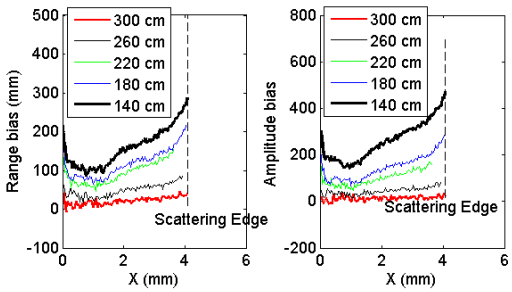

Figure 8: Scattering bias as a function of distance of the scattering object from the camera

Kavli et al. (2008) and Mure-Dubois and Hugli (2007) reported a maximum of 400 mm of range bias due to scattering based on their experiment. However, the scattering-induced range bias can reach up to 2500 mm in the presence of a highly reflective large surface area scattering object when the scattering and the background objects are separated at an appreciable distance.

Figure 9 shows the variation in range bias for two different scattering scene environments. In both the figures, it is clearly visible that the scattering-induced range bias is more in the periphery than the inside portion of the image plane. This is due to a greater power loss of the reflected signal at the periphery than in the middle portion of the imaging scene. The additional power loss of the SR3000 range camera at the periphery besides the cosine-fourth power loss observed in the standard optical system has been reported by Jaakkola et al. (2008).

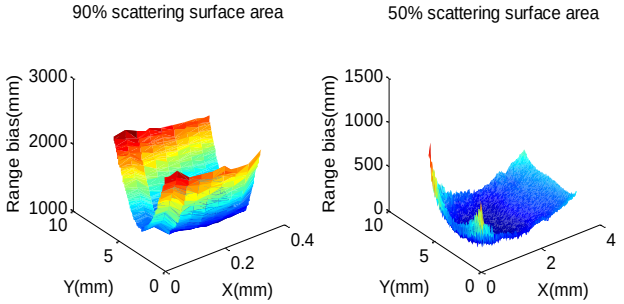

Figure 9: Camera at 1.4 m and 3.8 m from the scattering and background object respectively

3.2.2 SR4000 Range Camera

Chiabrando et al. (2009) have reported the absence of scattering distortions in an SR4000, which is the fourth generation range camera. However, it has been observed in this study that the scattering-induced biases exist but they are not as significant as in the SR3000. Figure 10 shows the ten-point moving average plot of the range and amplitude biases of one central row of pixels as a function of the surface area of the scattering object. The images were captured with the camera at 3.8 m from the background object and with the scattering object positioned at nine lateral positions at 2.2 m from the camera.

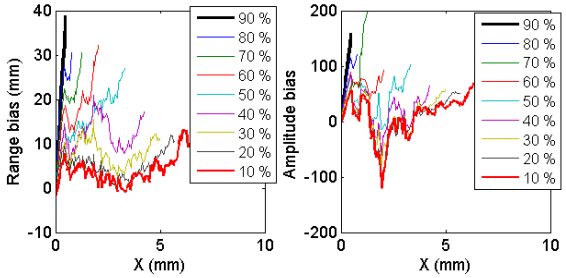

Figure 10: Scattering bias as a function of the surface area of the scattering object for SR4000

Figure 11 shows the scattering induced range and amplitude biases as a function of the distance of the foreground scattering object from the camera. These images were taken with the camera at 4.2 m from the background object with 50% surface area of the scattering object positioned at different distances from the camera. The maximum scattering-induced range bias in SR4000 is observed to 80 mm, which is within the noise of this camera for two consecutive frames. This shows that the scattering artefact in this camera is greatly reduced or eliminated as compared to the scattering bias observed in the SR3000.

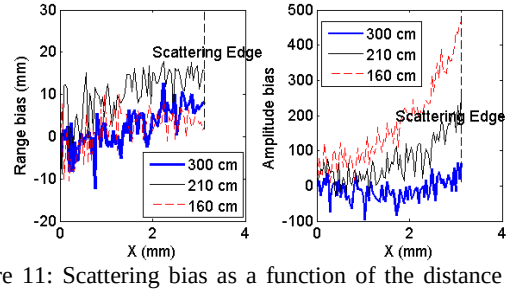

Figure 11: Scattering bias as a function of the distance of the scattering object from the camera for SR4000

4. METHODOLOGY OF SCATTERING COMPENSATION

This section describes a two-step process for scattering compensation. A 3D surface-fitting algorithm is used to smooth the noisy scattering range bias surface data. The smoothed surface is then used for scattering compensation using a cubic spline interpolation method.

4.1 Smoothing: 3D Surface Fitting

A generalized ridge estimator is used to fit a smooth surface to 3D grided data points. The elevation at the unknown data points are estimated using a linear interpolation on a triangular mesh as given in Equation 2, where P' is the desired elevation, P_1, P_2 and P_3 are the vertices of a triangle, and t and u are the scalars in x- and y-directions.

$$P' = P_1 + u * \overrightarrow{P_1P_2} + t * \overrightarrow{P_1P_3} \quad (2)$$

A smooth surface is achieved by a thin-plate bending mechanism where the minimization function is the potential energy of the extended springs connecting the plate and the data points, which is equivalent to the L2 norm. The smoothness parameter adjusts the fairing of the surface accordingly by bending rigidity of the plate and by shrinking or extending the springs. More on spring-plate approximation has been discussed in Yamada et al. (1999) and Greiner et al. (1996).

4.2 Interpolation: Cubic Spline

Using the surface fitting algorithm, smooth range-bias surfaces are obtained for different positions of the scattering object. Then a piecewise cubic polynomial interpolation is used to approximate the value for the required lateral or longitudinal distance using the corresponding pixel values from all the available smoothed surfaces. Mathematically, the cubic spline is modelled with the cubic polynomial in Equation 3 which is defined for each sub-interval $[x_i, x_{i+1}]$, where i = 1, 2,… N-1. For N number of points, there are N-1 cubic polynomials with 4(N-1) parameters.

$$F_i(x) = a_i + b_i(x - x_i) + c_i(x - x_i)^2 + d_i(x - x_i)^3 \quad (3)$$

Constraining Equation 3 with the following four conditions gives a unique solution:

1. The spline passes through all data points.
2. The first derivative is continuous at all interior points.
3. The second derivative is continuous at all interior points.
4. The boundary conditions at the end points are defined.

5. SCATTERING COMPENSATION MODEL

The range bias due to scattering is the subject of interest in this study. A range bias scattering compensation model based on the analytical curve-fitting method is proposed. Two different models were tested to compensate for the scattering-induced range bias on the background object.

5.1 Compensation Model I

Model I is a local compensation model defined only for a scattering object located at a particular distance from the camera where ancillary data of lateral scattering scenes are available for different percentage surface areas of the scattering object. The approximation of the required surface at a particular surface area of the scattering object is achieved by calculating values at each pixel location using the corresponding pixels values of the smoothed surfaces available at different locations of the scattering object. The not-a-knot spline interpolation is used to estimate the approximate surface.

Figure 12 shows the superimposed actual and approximated surfaces and success rate of the scattering compensation for Model I. The scattering compensation is tested for 55.7% surface area of the scattering object, when the scattering object and the background object are at 2.2 m and 3.8 m from the camera respectively. The success rate is calculated by computing the percentage difference of range bias between the actual and approximated range bias surfaces for all pixels independently. The achievement of this scattering compensation model is more than 80%, which corresponds to a maximum error of 21 mm. The high success rate for this model is due to the availability of dense data set for the lateral positions.

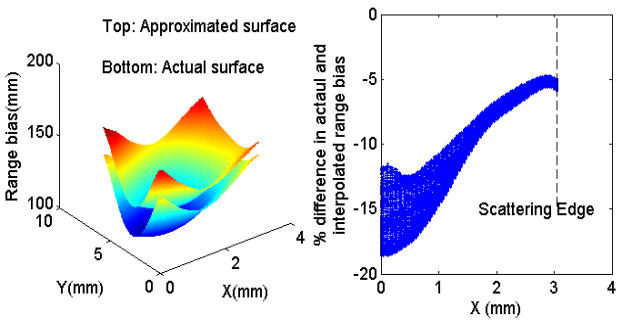

Figure 12: Scattering compensation for scattering object at 2.2m from the camera for Model I

5.2 Compensation Model II

Model II is a general compensation model defined for all distances of the scattering object from the camera with different percentage surface areas of the scattering object where ancillary data of both lateral and longitudinal scattering scenes are available. The approximation of the surface at the required distance of the scattering object from the camera for particular surface area of the scattering object is achieved in two steps. An intermediary surfaces at various distances for the required percentage surface area of the scattering object is computed using all the lateral and longitudinal scenes. Then from the intermediary surfaces obtained for the desired percentage surface area of the scattering object at different longitudinal distances, a new surface is interpolated at the required longitudinal distance of the scattering object from the camera. The pixel-wise interpolation in the above two steps is done using a not-a-knot spline interpolation.

Figure 13 shows the superimposed actual and approximated surfaces, and the success rate of the scattering compensation at 53.4% surface area of the scattering object when the scattering and background objects are at 2.2 m and 3.8 m from the camera respectively. This compensation model has accounted for more

than 60% of the scattering distortion which corresponds to a maximum error of 43 mm. The low success rate of this compensation model relative to Model I is due to only sparse ancillary data available for interpolation, which has biased the spline model.

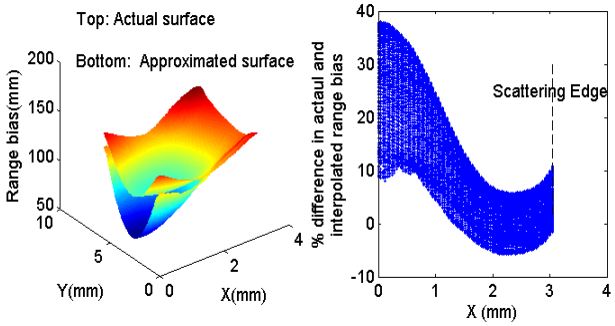

Figure 13: Scattering compensation for scattering object at 2.2 m from the camera for Model II

6. CONCLUSIONS AND FUTURE WORK

This paper presented the scattering effect observed in SR3000 and SR4000 range cameras using a two planar objects experiment. This study has shown that a highly reflective foreground object with a large scattering surface area can cause up to many order of magnitude errors (≈ 2500 mm) in the range measurements for the background objects. Empirically, it has been found that the scattering-induced range error is highly dependent on the surface area of the scattering object and the distance of the scattering object from the camera and the background scene. However, the scattering range bias is invariant to the integration time used to capture the scene. The range bias is seen to be more predominant at the periphery than the center of the image because of a greater loss of reflected power at the periphery.

An analytical scattering compensation model is presented with success rate ranging from 60% to 80%. Both Model I and Model II are pixel-wise scattering compensation models which uses the scattering data to interpolate a new correction surface by a cubic spline interpolation method. Model I produces a better result than the Model II, however, it cannot be used for global prediction of the scattering compensation. Model II can be used for the general prediction at different distances for different surface areas of the scattering object, but it requires dense scattering data in order to improve the accuracy of the spline interpolation. Future work will mainly deal with consolidating Model II for use in scattering compensation of the more complex scattering scene environments.

ACKNOWLEDGEMENTS

This work is supported by the Natural Sciences and Engineering Research Council of Canada (NSERC) and the University of Calgary.

REFERENCES

Beder, C. and Koch, R., 2008. Calibration of focal length and 3d pose based on the reflectance and depth image of a planar object, *International Journal of Intelligent Systems Technologies and Applications*, 5(3-4), pp. 285-294.

Chiabrando, F., Filiberto, R., Piatti, D. and Rinaudo, F., 2009. Sensors for 3d imaging- metric evaluation and calibration of a ccd/cmos time-of-flight camera, *Sensors*, 9(12), pp. 80–96.

Falie, D. and Buzuloiu, V., 2008. Further investigations on time-of-flight cameras distance errors and their corrections, 4th European Conference on Circuits and Systems for Communications, 10-11 July, pp. 197–200.

Greiner, G., Loos, J. and Wesselink, W., 1996. Data dependent thin plate energy and its use in interactive surface modeling, *Computer Graphics Forum*, 15(3), pp. 175–185.

Jaakkola, A., Kaasalainen, S., Hyypp, J., Niittymki, H. and Akujrvi, A., 2008. Intensity calibration and imaging with swissranger sr3000 range camera, *The International Archives of Photogrammetry, Remote Sensing and Spatial Information Sciences*, Vol. XXXVII Part B3a, pp. 155–160.

Kahlmann, T., Remondino, H. and Ingensand, H., 2006. Calibration for increased accuracy of the range imaging camera swissranger^{TM}, *Remote Sensing and Spatial Information sciences*, 36(5), pp. 136–141.

Karel, W., Dorninger, P. and Pfeifer, N., 2007. In situ determination of range camera quality parameters by segmentation, "Optical 3-D Measurement Techniques VIII", Zurich, Germany. http://www.ipf.tuwien.ac.at/publications /2007/Karel_Dorninger_opt3d.pdf (accessed 12 Feb. 2010).

Kavli, T., Kirkhus, T., Thielemann, J. T. and Jagielski, B., 2008. Modelling and compensating measurement errors caused by scattering in time-of-flight cameras, *Proc. SPIE: Two- and Three-Dimensional Methods for Inspection and Metrology VI*, 7066(1), pp. 4–13.

Lange, R., 2000. 3D Time-of-flight distance measurement with custom solid-state sensors in CMOS/CCD technology, PhD thesis, University of Siegen, Germany.

Lange, R. and Seitz, P., 2001. Solid-state time-of-flight range camera, *IEEE Journal of Quantum Electronics*, 37(3), pp. 390–397.

Lichti, D. D., 2008. Self calibration of 3d range camera, The International Archives of Photogrammetry, Remote Sensing and Spatial Information Sciences, Vol. XXXVII, pp. 927–932.

Mure-Dubois, J. and Hugli, H., 2007. Optimized scattering compensation for time-of-flight camera, *Proc. SPIE: The International Society for Optical Engineering*, Vol. 6762, p. 6762 0H.

Robbins, S., Murawski, B. and Schroeder, B., 2009. Photogrammetric calibration and colorization of the swissranger sr3100 3d range imaging sensor, *Optical Engineering*, 48(5), pp. 1–8.

Yamada, A., Furuhata, T., Shimada, K. and Hou, K., 1999. A discrete spring model for generating fair curves and surfaces, "Seventh Pacific Conference on Computer Graphics and Applications", Seoul, Korea. http://www.computer.org/portal/ web/csdl/doi/10.1109/PCCGA.1999.803371 (accessed 10 Feb. 2010).